



Efficient and selective electrochemical reduction of nitrate to N₂ by relay catalytic effects of Fe-Ni bimetallic sites on MOF-derived structure

Jie Sun ^a, Weiqi Gao ^a, Honghan Fei ^{a,*}, Guohua Zhao ^{a,b,**}

^a School of Chemical Science and Engineering, Shanghai Key Lab of Chemical Assessment and Sustainability, Tongji University, Shanghai 200092, People's Republic of China

^b Institute of Translational Research, Shanghai Tongji Hospital, Tongji University, Shanghai 200092, People's Republic of China



ARTICLE INFO

Keywords:

Nitrate reduction
Electrochemical reduction
Bimetallic sites
Relay catalytic effect
Water treatment

ABSTRACT

Selective electrocatalytic conversion of NO₃⁻ to N₂ is an environmental-friendly strategy to close the anthropogenic nitrogen-based cycle. This work reported a metal-organic framework-derived electrocatalyst with earth-abundant bimetallic sites, showing quantitative (~97.9% conversion) and selective (~99.3%) nitrate-to-N₂ transformation. More importantly, both post-catalysis concentrations of NO₃⁻ and NO₂⁻ meet the drinking water limit requirements, set by World Health Organization. The reaction intermediates and mechanistic pathways in electrocatalytic reduction of NO₃⁻ to N₂ are elucidated by a variety of in-situ experimental studies and DFT calculations. The enhanced and selective electrocatalytic performances are ascribed to the relay catalytic effects of the neighboring Fe-Ni catalytic sites residing in the porous carbon electrocatalysts, which are structurally determined by X-ray absorption spectroscopy (XAS) as well as calculated structural model, with Fe sites decreasing the reaction barrier for NO₃⁻ conversion and Ni centers facilitating the adsorption and activation of reaction intermediates (NO₂⁻, NO^{*} and N₂O^{*}).

1. Introduction

Closing the nitrate-nitrogen cycle has attracted widespread attention, owing to the anthropogenically-induced rapid increase in environmental nitrate (NO₃⁻) concentration such as fertilizer-intensive agriculture and industrial productions [1–4]. The inorganic nitrogen pollution (NO₃⁻, NO₂⁻ and NH₄⁺) are known to cause a variety of human health hazards (e.g. methemoglobinemia and non-Hodgkin's lymphoma) [5]. Indeed, the World Health Organization (WHO) has established the limiting concentrations of NO₃⁻, NO₂⁻, and NH₄⁺ in drinking water since 2011, which are 10, 0.03, and 0.4 mg N/L, respectively [6, 7]. A number of physical and chemical technologies, including ion exchange, reverse osmosis and chemical catalysis, have been developed to perform the nitrate reduction, but suffering from slow reaction kinetics, extensive by-products as well as expensive and unsafe utilization of H₂ [8–12]. Therefore, it is highly desirable to develop an efficient, selective and environmentally friendly strategy to transform NO₃⁻ to harmless nitrogen (N₂).

Very recently, electrocatalytic NO₃⁻ reduction has been developed to

be an alternative and promising approach because of its moderate operation conditions and good efficiency [6,13–17]. Electrocatalytic transformation involves a stepwise reaction with a rate-determining step of the reduction of NO₃⁻ to NO₂⁻, followed by a selectivity-determining step to further reduce NO₂⁻ to other nitrogen species [18,19]. In contrast to single noble metal system, bimetallic electrocatalytic systems often have synergistic effects with one metal catalytically active site contributing to the activation of NO₃⁻ (i.e. the rate-determining step) while the other metal performing the conversion of intermediate NO₂⁻ (i.e. the selectivity-determining step) [20–22]. However, the previously reported electrocatalysts need precise metals (e.g. Pd) or long reaction time and often have metal leaching problems as well, limiting their practical applications in NO₃⁻ removal. More importantly, the bottlenecks of electrocatalytic NO₃⁻ reduction lie in controlling the selectivity of products, investigating the reaction mechanism and the direct observation of intermediate products, which have not been well resolved for more than half a century [23,24].

Metal-organic frameworks (MOFs) are an emerging class of promising electrocatalytic materials, owing to their tunable porosity,

* Corresponding author.

** Corresponding author at: School of Chemical Science and Engineering, Shanghai Key Lab of Chemical Assessment and Sustainability, Tongji University, Shanghai 200092, People's Republic of China.

E-mail addresses: fei@tongji.edu.cn (H. Fei), g.zhao@tongji.edu.cn (G. Zhao).

ultrahigh surface area and versatile functionalities [25–27]. The confined porosity residing in MOFs serve as individual nanoscale reactors to enhance the host-guest interactions, facilitating the activation of catalytic substrates [28,29]. More importantly, MOF-derived porous carbon materials often show high electrical conductivity while retaining the porous topology, therefore lowering the charge-transfer energy barriers of many parent MOFs [30,31]. Therefore, many MOF-derived N-doped carbon materials show high electrocatalytic performances in CO₂ reduction [32], oxygen reduction [33] and hydrogen evolution reactions [34]. For example, Jiang et al. reported the Ni-N₃-C species in porous MOF-derived structure greatly reduce the formation energy of COOH*, which is the rate-determining step for electrocatalytic CO₂ reduction [25].

Herein, we report a MOF-derived nitrate reduction electrocatalyst with earth-abundant Fe-Ni-N₆ coordination centers. The coordination structure of Fe and Ni metals with N not only makes the metal highly dispersed and increases the catalytic active sites, but also avoids the metal leaching and improves the stability of the material. The extremely short distance between Fe and Ni species facilitates the transfer of nitrite from Fe to the Ni surface to achieve efficient relay catalysis, thereby improving the selectivity of nitrogen.

2. Experimental section

2.1. Reagents and chemicals

Zinc nitrate hexahydrate (Zn(NO₃)₂·6H₂O, ≥ 99%), iron nitrate nonahydrate (Fe(NO₃)₃·9H₂O, ≥ 99%), nickel nitrate hexahydrate (Ni (NO₃)₂·6H₂O, ≥ 99%), sodium nitrate (NaNO₃, ≥ 99%), potassium nitrate (KNO₃, ≥ 99%), hydrochloric acid (HCl, 37%), trichloromethane (CHCl₃, ≥ 99%), and ethanol (C₂H₆O, ≥ 99.8%) were purchased from Sinopharm Chemical Reagent Co., Ltd., SCRC, China. 2-Methylimidazole (C₄H₆N₂, ≥ 98%), N-(1-Naphthyl) ethylenediamine dihydrochloride (C₁₂H₁₆Cl₂N₂, ≥ 99%), and potassium sodium tartrate (NaKC₄H₄O₆·4H₂O, ≥ 99.5%) were purchased from Sigma-Aldrich Chemical Reagent Co., Ltd., China. Methanol (CH₄O, ≥ 99.8%), n-hexane (C₆H₁₄, ≥ 95%), sodium nitrite (NaNO₂, ≥ 99%), phosphoric acid (H₃PO₄, ≥ 85%), and Nafion solution (~5%) were purchased from Shanghai Mike Lin Biochemical Technology Co., Ltd. Sulfamic acid (NH₂SO₃H, ≥ 99.9%), and Nessler's reagent (HgI₄K₂, ≥ 98%) were purchased from Aladdin Industrial Inc. P-aminobenzenesulfonamide (C₆H₈N₂O₂S, ≥ 99%) and ammonium chloride (NH₄Cl, ≥ 99.8%) were purchased from Adamas Reagent Co., Ltd. All chemicals were used without further purification. The ultrapure water required for preparation of all working solution was purified by Milli-Q system (Milli-pore, USA > 18.0 MΩ).

2.2. Preparation of Fe₃Ni-N-C

In a typical procedure, 100 mg of Fe doped ZIF-8 was dispersed in 12 mL of n-hexane and the solution was under ultrasound at room temperature for 1 h to form a homogeneous suspension. Then, the methanol solution containing Ni(NO₃)₂ (25 mg/mL, 47 μL) was added to the suspension and under ultrasound at room temperature for 10 min. Next, the suspension was stirred at room temperature for another 1 h. The as-synthesized precipitates were centrifuged and washed with methanol for several times and then placed in vacuum at 60 °C overnight to obtain the Fe₃Ni doped ZIF-8. Finally, the Fe₃Ni doped ZIF-8 was placed in a tube furnace and heated to 1000 °C for 1 h in a stream of Ar to yield Fe₃Ni-N-C. The synthesis of Fe_xNi_y-N-C (x:y = 1:2, 1:1, 2:1, 4:1) was prepared by changing the ratio of Fe(NO₃)₃·9H₂O to the methanol solution containing Ni(NO₃)₂.

2.3. Characterization methods

The structure and morphology of the catalysts were characterized by

field emission scanning electron microscope (FE-SEM, Hitachi S-4800) and high resolution transmission electron microscope (HR-TEM, JEM 2100), and energy dispersive X-ray spectroscopy mapping (EDS-mapping) was obtained through Energy Dispersive X-Ray Spectrometer. Powder X-ray diffraction (PXRD) was measured by Bruker D8 Advance X-ray diffractometer. Thermogravimetric (TGA) and differential scanning calorimetry (DSC) tests were performed on Thermo Scientific FLASH 2000 NC Analyzer equipment under air atmosphere. The metal contents of the catalysts were obtained by inductively coupled plasma emission spectroscopy (ICP-OES, SPS3520UV-DD, SII Nano Technology Inc., Japan). N₂ adsorption-desorption isotherms test was carried out at 77 K with the Micromeritics TriStar 3020 instrument. The sample was degassed at 473 K overnight before the test. The specific surface area of the materials was calculated from the selected N₂ adsorption-desorption isotherms in the relative pressure range of 0.05–0.2. The pore size distribution was obtained by performing the BJH method on the adsorption branch. Ultraviolet-visible absorption spectra were obtained on the Agilent 8453 ultraviolet and visible spectrophotometer. The valence state and bonding structure of the elements were determined by X-ray photoelectron spectroscopy (XPS, Thermo ESCALAB250 with K_α radiation). X-ray absorption near-edge structure (XANES) and extended X-ray absorption fine structure (EXAFS) data were collected on the 11B beamline of the Shanghai Synchrotron Radiation Facility (SSRF). Differential electrochemical mass spectrometry (DEMS, QAS 100) was provided by Shanghai Linglu Instrument Co., Ltd. for online analysis of intermediates and products in NO₃⁻ reduction reaction. The amount of hydrogen produced on the cathode was calculated by use of gas chromatography (GC7900, Shanghai Timi). For all tests, the gas sample (1 mL) was pumped into the GC in the headspace position of the cathode via off-line sampling.

2.4. Nitrate reduction experiments

Electrocatalytic NO₃⁻ reduction reactions were carried out in a three-electrode electrochemical reaction cell with a volume of 5 mL (Fig. S1), and were monitored by the CHI660C electrochemical workstation (CH Instruments Inc., USA). A Pt wire was used as the counter electrode, a saturated calomel electrode was used as the reference electrode, and a magnetic stirrer was used in all reactions to increase the diffusion rate during the reaction. All recorded potentials were relative to the reference electrode. To prepare the working electrode, 5 mg of catalyst and 10 μL of Nafion (5%) solution were added to 1 mL of deionized water by ultrasonic dispersion for 1 h to mix the catalyst. Then the as-prepared ink was drop-coated onto the FTO conductive glass (1 cm × 1 cm). The working electrode was then dried at room temperature for subsequent electrochemical tests. Linear sweep voltammetry (LSV) tests were carried out at a sweep rate of 2 mV s⁻¹ within the potential range from 0 to -1.6 V vs. SCE. I-t-test was performed in a solution containing 100 ppm NaNO₃-N and 0.1 M Na₂SO₄ at a continuous potential of -1.3 V vs. SCE for 5 h. Electrochemical impedance spectroscopy (EIS) tests were also performed in a solution containing 100 ppm NaNO₃-N and 0.1 M Na₂SO₄ at a frequency of 10⁻² to 10⁶ Hz. Cyclic voltammetry (CV) tests were performed at a scan rate of 20–100 mV s⁻¹ within the potential range from 0.1 to 0.4 V vs. SCE. The quantification of ECSA was carried out by measuring the double-layer capacitance at the electrode-electrolyte interface.

2.5. In-situ IR measurements

5 mg of catalyst and 10 μL of Nafion (5%) solution were added to 1 mL of deionized water by ultrasonic dispersion for 1 h to obtain the catalyst ink. The ink dispersion was then uniformly drop-coated onto the glassy carbon electrode. The working electrode was mounted in a single-chamber three-electrode spectroelectrochemical cell with a platinum wire as the counter electrode and a saturated calomel electrode as the reference electrode. In-situ IR spectra were measured on a Nicolet 8700

FTIR spectrometer, equipped with an MCT cryogenic detector with resolution of 8 cm⁻¹. All in-situ electrochemical IR tests were controlled by CHI660C electrochemical workstation (CH Instruments Inc., USA) in a solution containing 100 ppm NaNO₃-N and 0.1 M Na₂SO₄. The activation of the working electrode was carried out by repeatedly running cyclic voltammetry within the potential range from -0.1 to -1.5 V vs. SCE with a rate of 2 mV s⁻¹ until a stable CV curve could be obtained. Then the electrochemical measurements were performed within the potential range from -0.1 to -1.3 V vs. SCE at a scan rate of 2 mV s⁻¹.

2.6. Differential electrochemical mass spectrometry (DEMS) measurements

2000 ppm N-NaNO₃ with 0.1 M Na₂SO₄ electrolyte was kept flowing into a specially-made electrochemical cell through a peristaltic pump. Ar was bubbled into the electrolyte constantly before and during the DEMS measurements. A glassy carbon electrode coated with Fe₃Ni-N-C, a Pt wire electrode, and a saturated calomel electrode were used as the working electrode, the counter electrode and the reference electrode, respectively. LSV test was employed from 0 to -1.6 V vs. SCE at a scan rate of 10 mV s⁻¹ until the baseline kept steady. Then, the corresponding mass signals appeared. After the electrochemical test was over and the mass signal returned to baseline, the next cycle started using the same test conditions to avoid the accidental error during DEMS measurements. The experiment ended after four cycles.

2.7. Density functional theory (DFT) calculations

All of the spin-polarized DFT calculations were performed using the VASP program [35], which uses a plane-wave basis set and a projector augmented wave method (PAW) for the treatment of core electrons [36]. The electronic interaction was described by the standard PAW potential. The valence configurations of H, C, N, O, Fe, and Ni were 1s¹, 2s²2p², 2s²2p³, 2s²2p⁴, 3d⁶4s², and 3d⁸4s², respectively. The Perdew, Burke, and Ernzerhof exchange-correlation functional within a generalized gradient approximation (GGA-PBE) was used in our calculations, and the van der Waals (vdW) correction proposed by Grimme (DFT-D3) was employed due to its good description of long-range vdW interactions [36]. For the expansion of wavefunctions over the plane-wave basis set, a converged cutoff was set to 450 eV.

In order to simulate a carbon catalyst doped with metal-nitrogen, a 4 × 2 graphene superlattice with periodic boundary conditions ($a = 9.84 \text{ \AA}$, $b = 8.52 \text{ \AA}$) was used, and then some carbon atoms were removed to form Fe-N₄, Ni-N₄ and N-coordinated Fe-Ni bimetallic sites. The vacuum space in the z direction was set to be greater than 18 Å to avoid interaction between periodic images. During the geometric optimization, all atomic coordinates were completely relaxed until the remaining atomic force was less than 0.01 eV/Å, and the total energy was converged to 10⁻⁵ eV. The Brillouin zone integration was performed on a (5 × 6 × 1) Monkhorst-Pack grid.

The free energy change of each electrochemical step involved in the proton-electron transfer was calculated based on the calculated hydrogen electrode (CHE) model, and the free energy of (H⁺ + e⁻) was equal to 1/2 H₂ (g) for the standard hydrogen electrode (SHE). The free energy of adsorbed and non-adsorbed substances is calculated by the Eq. (1):

$$\Delta G = \Delta E + \Delta E_{ZPE} - T\Delta S \quad (1)$$

Where ΔE is the electron energy calculated by DFT, ΔE_{ZPE} is the zero point energy (ZPE), T is temperature, and ΔS is entropy [37]. The ΔS and ΔE_{ZPE} of free molecules and adsorbents were calculated from the vibration frequency. In order to describe charged NO₃⁻ (as a reference), a neutral HNO₃ gas was selected as a substitute for NO₃⁻ and the energy of NO₃⁻ was obtained in the thermodynamic cycle to avoid the difficulty of periodic DFT calculations for charged systems.

The mechanism of the hydrogen evolution reaction (HER) was evaluated by a three-state diagram containing the initial H⁺ state, the intermediate H^{*} state, and the final 1/2 H₂ state. The free energy of the intermediate H^{*} state (ΔG_{H^*}) is considered to be a key indicator of the HER activity of the electrocatalyst. An electrocatalyst with a positive value leads to low kinetics of adsorption of H₂, while a catalyst with a negative value leads to low kinetics of release of H₂. The ΔG_{H^*} is calculated by the Eq. (2) [38]:

$$\Delta G_{H^*} = \Delta E_{H^*} + \Delta E_{ZPE} - T\Delta S_H \quad (2)$$

Where ΔE_{H^*} represents the binding energy of adsorbed hydrogen, ΔE_{ZPE} and ΔS_H represent the difference between the ZPE and entropy of hydrogen adsorbed and hydrogen in the gas phase, respectively. Since the vibrational entropy of hydrogen in the adsorption state is negligible, $\Delta S_H \approx -\frac{1}{2}S_{H_2} \text{ (g)}$, where S_{H_2} represents the entropy of hydrogen in the gas phase under standard conditions, so the above Equation can be described as Eq. (3) [39]:

$$\Delta G_{H^*} = \Delta E_{H^*} + 0.24 \text{ eV} \quad (3)$$

3. Results and discussion

3.1. Characterization of the composite cathode

Fe-Ni bimetallic porous carbon catalyst was prepared through the mixed-metal synthesis and encapsulation strategy based on the pyrolysis of Zn/Fe/Ni zeolitic imidazolate framework (ZIF-8) (Fig. 1a). Highly crystalline ZIF-8 with a SOD net topology, consisting of Zn²⁺ ions as nodes and 2-methyl-imidazole as organic linkers, was synthesized by mixing Zn(NO₃)₂ and 2-methyl-imidazole in MeOH at room temperature [40]. Fe³⁺-doped ZIF-8 (ZIF-8(Zn/Fe)) was synthesized by using Fe (NO₃)₃ as a second metallic source in a similar manner [41]. Both materials exhibit the highly porous SOD topology, as verified by powder X-ray diffraction (PXRD) and pore size distribution (Fig. 1b and Fig. S2). BET surface areas of ZIF-8 and ZIF-8(Zn/Fe) were determined to be 1864 m²/g and 1823 m²/g using N₂ at 77 K (Fig. 1c), suggesting Fe³⁺ residing in the MOF nodes instead of trapped in the porosity. The encapsulation of Ni(NO₃)₂ in ZIF-8(Zn/Fe) was performed in mixed solution of hexane and MeOH, followed by activation at 60 °C under vacuum [42]. The Ni²⁺-encapsulated material (ZIF-8(Zn/Fe/Ni)) was confirmed to maintain the crystalline ZIF framework, but a reasonable decrease in BET surface area from 1823 m²/g to 1560 m²/g was observed.

Annealing ZIF-8(Zn/Fe/Ni) at 1000 °C under Ar atmosphere decomposed the organic linkers as well as volatilized Zn²⁺ species with a low boiling point of 907 °C, affording Fe/Ni bimetallic nitrogen-doped porous carbon materials (Fe₃Ni-N-C). Field-emission scanning electron microscopy (SEM) suggests Fe₃Ni-N-C retaining the typical dodecahedra morphology of ZIF-8 with particle size of ~100 nm (Fig. 2a and b, and Fig. S3). To note, PXRD confirms Fe₃Ni-N-C occupying graphite carbon structure with characteristic broad peaks at 25° and 44° but no observed Fe/Ni metallic phases (Fig. 1b and Fig. S4). Moreover, high-resolution transmission electron microscopy (HRTEM) indicates Fe₃Ni-N-C has a polyhedral morphology with no obvious aggregated Fe/Ni metallic particles residing in the porous carbon structure, again suggesting the highly dispersed metal active sites in the porous carbon matrix (Fig. 2c and d). Selected area electron diffraction (SAED) pattern demonstrates the amorphous nature of porous Fe₃Ni-N-C material (Fig. 2d inset). The high porosity was further examined by N₂ sorption isotherms at 77 K, showing a high BET surface of 996 m²/g and obvious contours of hysteresis loops (Fig. 1c). This phenomenon confirms the retention of MOF microporosity upon the high-temperature carbonization treatment. The metallic contents of Fe and Ni in the resultant Fe₃Ni-N-C were measured to be 0.93 wt% and 0.36 wt%, evidenced by inductively coupled plasma

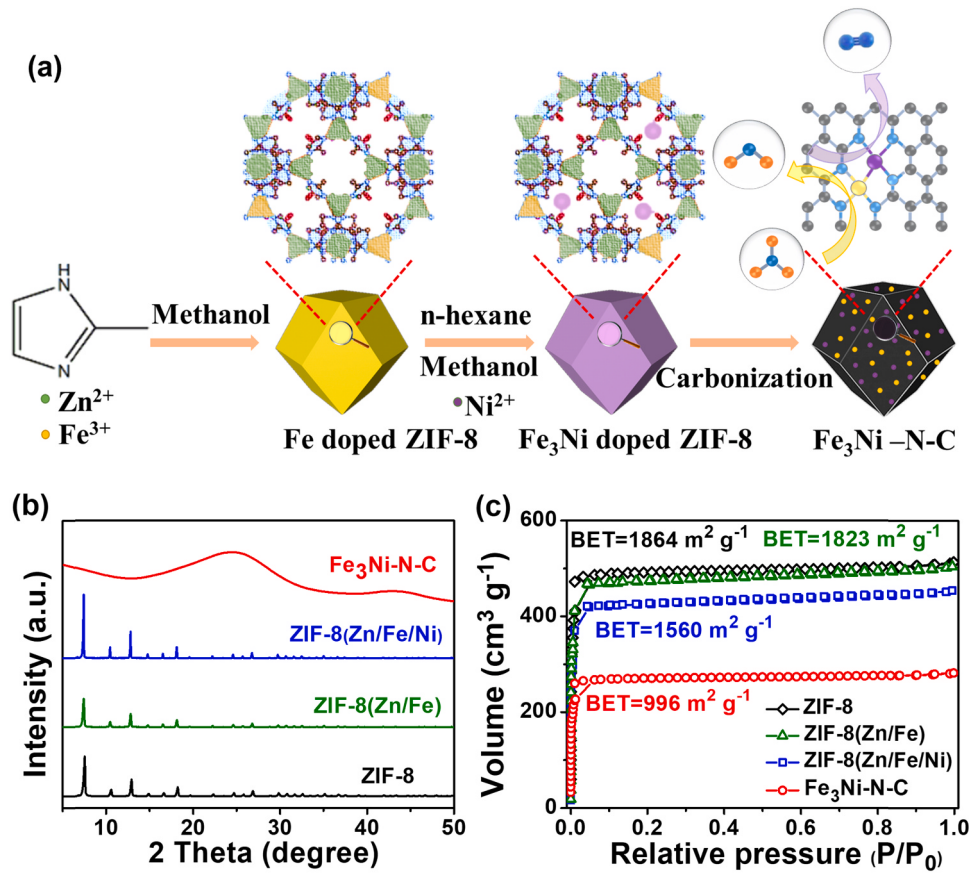


Fig. 1. (a) Synthetic scheme of Fe₃Ni-N-C cathode materials. (b) PXRD patterns and (c) N₂ adsorption–desorption isotherms of ZIF-8, ZIF-8(Zn/Fe), ZIF-8(Zn/Fe/Ni), and Fe₃Ni-N-C.

optical emission spectrometer (ICP-OES) (Table S1). Elemental compositions were also verified by thermogravimetric (TGA) and differential scanning calorimetry (DSC) tests (Fig. S5). In addition, the elemental mapping by energy dispersive X-ray spectroscopy (EDS-mapping) indicates both metal centers and doped nitrogen species are uniformly distributed on the porous carbon substrate within a single dodecahedra microcrystal (Fig. 2e). To note, tuning the concentration of metallic precursors will incorporate different ratios of the bimetallic species (Fe/Ni) into the N-doped carbon, affording full compositional range from pure Fe to Ni end-members, namely Ni-N-C, Fe-N-C, FeNi-N-C, FeNi₂-N-C, Fe₂Ni-N-C, Fe₃Ni-N-C, and Fe₄Ni-N-C, respectively (Table S2).

In order to study the structure of active catalytic sites, XAS has been employed to investigate the fine structure of bimetallic species residing in Fe₃Ni-N-C. First, X-ray absorption near-edge structure (XANES) spectra indicates that the valence state of Fe in Fe₃Ni-N-C locating between Fe⁰ (Fe foil) and Fe³⁺ (Fe₂O₃) with a front edge feature of ~7110 eV, implying the hybridization of 3d and 4p orbitals of Fe centers (Fig. 2f) [43]. The higher peak intensity of Fe₃Ni-N-C was attributed to the symmetric distortion of D_{4h} coordination environment, suggesting the possible Fe to metal coordination [43]. Moreover, Fe K-edge Fourier transform (FT) k²-weighted extended X-ray absorption fine structure (EXAFS) spectra of Fe₃Ni-N-C provide two prominent bands at 1.51 Å and 2.06 Å, corresponding to the first neighboring atoms of coordinating N and the possible formation of dinuclear Fe-Ni centers, respectively (Fig. 2g) [44]. Meanwhile, Ni K-edge Fourier transform (FT) k²-weighted EXAFS spectra of Fe₃Ni-N-C reveals analogous coordination environment with Ni-N coordination at 1.74 Å and Ni-Fe distance at 2.08 Å (Fig. S6) [25]. The set of data was best fit using a possible Fe-Ni dinuclear structure model with a reasonable R-factor of 0.008, which was simulated by DFT calculations (Fig. 2h). In this case, the FeNiN₆ catalytic center consists of both Fe and Ni centers in a distorted square

planar coordination environment (Table S3). Indeed, the peak fitting of high-resolution N 1s X-ray photoelectron spectroscopy (XPS) of Fe₃Ni-N-C indicates the existence of metal-nitrogen bonds (399.6 eV), which agrees with the proposed structure with dinuclear metal centers anchored by N atoms (Fig. S7) [45].

3.2. Electrochemical nitrate reduction on the composite cathode

Electrocatalytic reduction of nitrate was performed in a three-electrode single-chamber electrochemical reaction cell, and a series of electrochemical tests were performed on the electrocatalysts to evaluate the NO₃⁻ removal rate and N₂ selectivity. The choice of a single-chamber cell is suitable in our case, because the oxidation of by-product NH₄⁺ to N₂ on the Pt anode will not occur under neutral condition (pH~7) [46, 47]. Moreover, the same experimental setup will achieve direct comparison with the catalytic activities of many reported literatures for electrocatalytic nitrate reduction [7, 14]. The reactant and reductive products including NO₃⁻, NO₂⁻, NH₄⁺, and N₂ were detected using colorimetric methods (Fig. S8). As shown in Fig. 3a, a reversible oxidation peak was generated when the applied cathode potential was 1.0 V vs. SCE, which means that the Fe species were oxidized. These results indicate that the onset potentials as scanning in negative direction are ascribed to the reduction of Fe³⁺. At the same time, we can observe that there will be an obvious reduction peak only in the electrolyte containing nitrate (Fig. 3b), indicating that this reduction peak is caused by the reduction of Fe and nitrate. Among the obtained N-doped carbon materials with bimetallic species (Fe/Ni), Fe₃Ni-N-C electrocatalysts exhibited the highest and nearly quantitative NO₃⁻ removal rate (97.9%), N₂ selectivity (99.3%), and Faradaic efficiency (52.1%) within 30 min (Fig. 4a). These values are substantially higher than all of the previously reported electrocatalysts, superior to other bimetallic

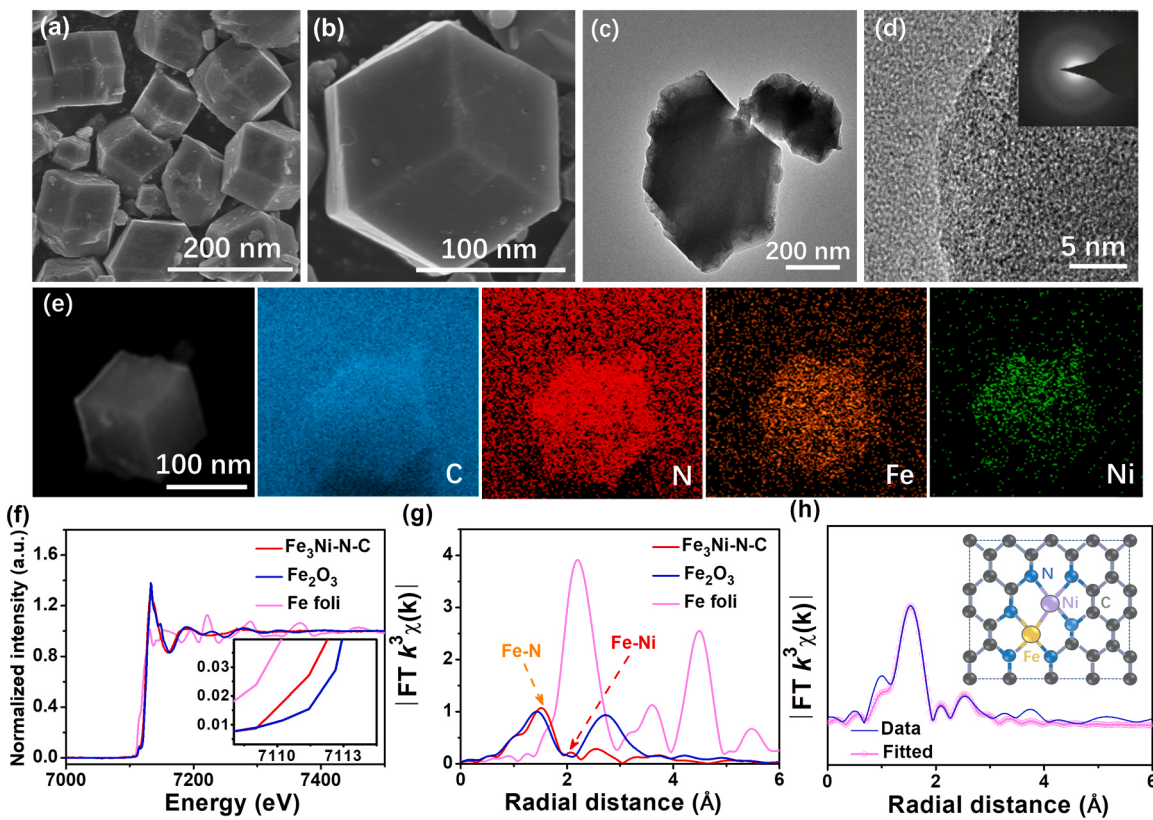


Fig. 2. (a, b) SEM images, (c) TEM image, (d) HRTEM image (inset: SAED), and (e) EDS-mapping of $\text{Fe}_3\text{Ni-N-C}$. (f) Fe k-edge XANES spectra and (g) Fourier-transformed EXAFS spectra at R space of $\text{Fe}_3\text{Ni-N-C}$, Fe_2O_3 , and Fe foil. (h) EXAFS fitting of $\text{Fe}_3\text{Ni-N-C}$ and optimized coordination environment of Fe and Ni atoms (inset).

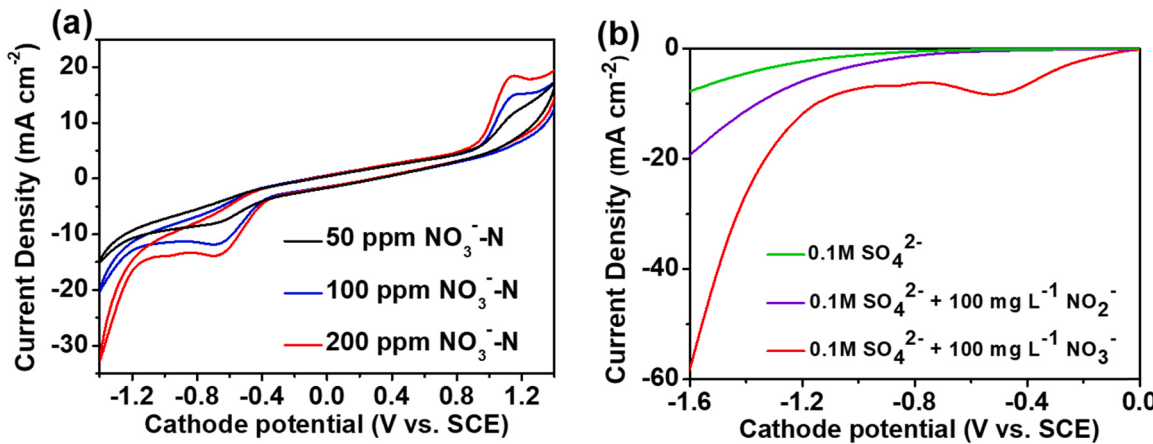


Fig. 3. (a) CV curves of $\text{Fe}_3\text{Ni-N-C}$ in different concentrations of nitrate recorded at 50 mV s^{-1} . (b) LSV curves of $\text{Fe}_3\text{Ni-N-C}$ under different electrolyte conditions.

electrocatalysts as well as those containing precise metals (Table S4) [48,49]. Meanwhile, the single metallic counterparts (Fe-N-C and Ni-N-C) showed a much lower NO_3^- removal rate (27–35%) and N_2 selectivity (36–49%), suggesting the possible relay catalytic effects of Fe and Ni species. The change of inorganic nitrogen ion concentrations during the reaction was tested to investigate the possible reaction pathway (Fig. 4b). First, the concentration of NO_3^- gradually decreased to an extremely low level of 2.1 ppm NO_3^- -N within 30 min. Meanwhile, the concentration of NO_2^- slowly increased during the first 5 min, followed by decreasing to 0.3 ppm NO_2^- -N in the next 25 min. These results indicated the initial reaction pathway of the conversion of NO_3^- to NO_2^- , followed by the rapid turnover from NO_2^- to N_2 . No presence of

NH_4^+ as well as other by-products were observed. Importantly, both post-catalysis NO_3^- and NO_2^- concentrations meet the WHO requirement for drinking water limit. The onset potential of $\text{Fe}_3\text{Ni-N-C}$ ($\sim 0.0 \text{ V}$ vs. SCE) was substantially lower than that of Fe-N-C or Ni-N-C cathodes ($\sim -0.3 \text{ V}$ vs. SCE) (Fig. 4c). Moreover, the electrochemical impedance spectroscopy (EIS) evidenced that the bimetallic $\text{Fe}_3\text{Ni-N-C}$ has a smaller Nyquist plot diameter than single-metallic electrocatalytic materials, implying the high charge transfer ability of $\text{Fe}_3\text{Ni-N-C}$ (Fig. 4d). As shown in Fig. 5a, Faradaic efficiency was elevated from 26.5% to 80.3% when cathodic potentials altered from -1.0 to -1.3 V vs. SCE, indicating favorable kinetics for nitrate reduction at a low cathode potential. At -1.4 V , Faradaic efficiency substantially dropped down to 52.3%

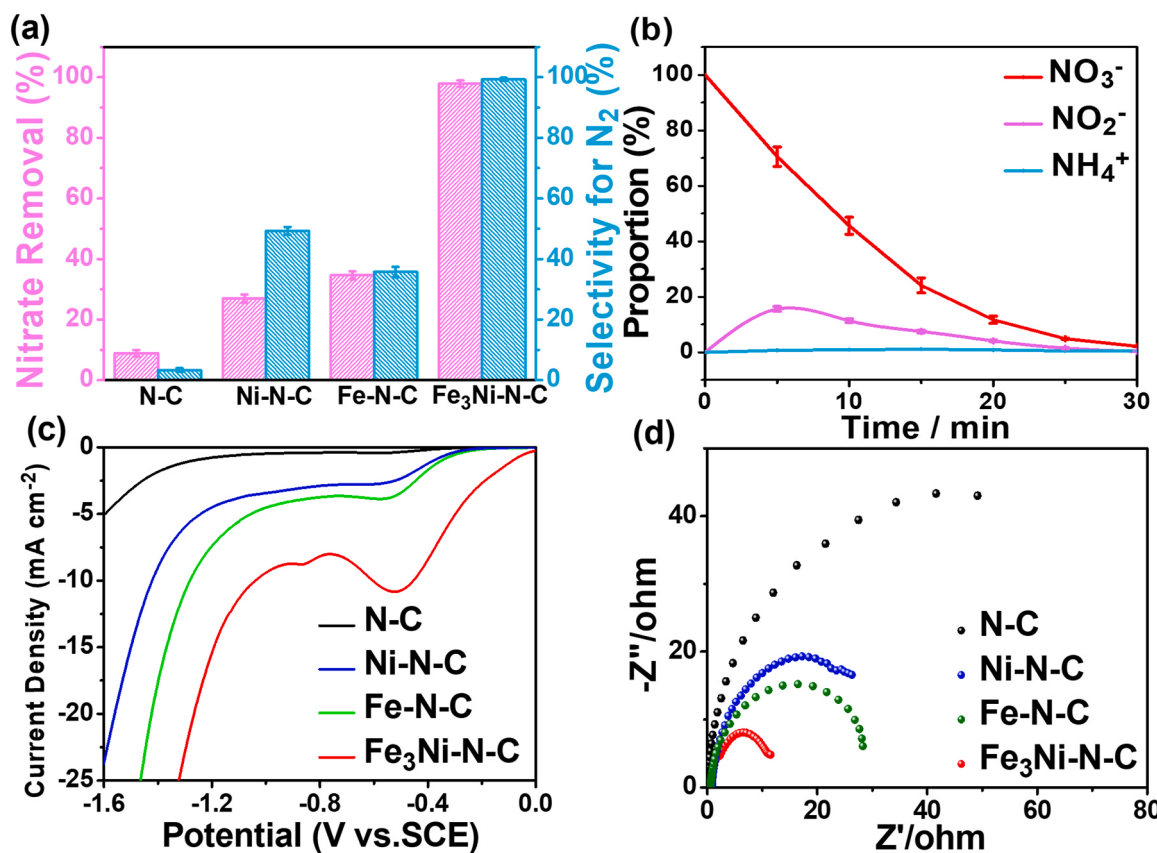


Fig. 4. (a) NO₃⁻ removal rate and N₂ selectivity of N-C, Ni-N-C, Fe-N-C, and Fe₃Ni-N-C. (b) Concentrations of NO₃⁻, NO₂⁻ and NH₄⁺ plotted as a function of reaction time over Fe₃Ni-N-C. (c) LSV curves and (d) EIS plots of N-C, Ni-N-C, Fe-N-C, and Fe₃Ni-N-C (5 mL of electrolyte: 100 ppm NaNO₃-N, 0.1 M Na₂SO₄, the applied potential is -1.3 V vs. SCE, 30 min).

due to the electrolysis of water to hydrogen. The Fe₃Ni-N-C is a very effective cathode material, with a mean Energy consumption of only ~35 kWh/kg NO₃⁻. Energy consumption increases as the reaction time increases, due to the decrease of nitrate in the electrolyte and more electrical energy is used to produce hydrogen (Fig. 5b). We have compared the electrocatalytic nitrate reduction performance with nickel foam (1 cm × 1 cm), iron foam (1 cm × 1 cm) and plated Fe-Ni alloys (1 cm × 1 cm). The Fe-Ni alloys are prepared by in-situ reduction of iron using nickel foam as the cathode material in an electrolyte containing iron nitrate. As shown in Fig. 5c, compared with these three kinds of electrodes, Fe₃Ni-N-C electrode shows more excellent nitrate conversion rate and nitrogen selectivity.

Metal electrocatalysts often undergo corrosion during the electrolysis process and cause secondary metal pollution, therefore the long-term stability of the electrocatalysts is equally important to evaluate the practical application of metal electrocatalysts. Fe₃Ni-N-C exhibited high stability over 10 continuous electrocatalytic cycles in the electrolyte containing 100 ppm NaNO₃-N and 0.1 M Na₂SO₄ at -1.3 V vs. SCE. Negligible loss in both NO₃⁻ removal rate (> 95%) and N₂ selectivity (> 98%) was observed. Besides, the leaching mass of metal ions is very low after the reaction and this value will decrease with the increase of the number of cycles. These results prove that the Fe₃Ni-N-C catalyst can remain stable over multiple cycles and the bimetal can be stably anchored to the catalyst by the metal-N coordination (Fig. 5d). Indeed, no decrease in current intensity ($i \sim t$) was noted over a continuous electrocatalytic span of 5 h, evidencing the catalytic activity largely maintained throughout the long-term reaction (Fig. S12). The crystallinity and dodecahedral morphology of Fe₃Ni-N-C were also retained after the 10-cycle NO₃⁻ reduction reactions (NRR), confirmed by PXRD and SEM, respectively (Figs. S13 and S14). In order to further study the

electrocatalytic performance of Fe₃Ni-N-C in a large-scale aqueous condition, a 100 mL of electrolyte containing 100 ppm NaNO₃-N and 0.1 M Na₂SO₄ was employed (Fig. S15). Fe₃Ni-N-C maintains a high NO₃⁻ removal rate of 86.6% and a N₂ selectivity of 89.9% within a catalytic period of 5 h. Overall, the above-mentioned results indicate that Fe₃Ni-N-C has high catalytic activity, selectivity and durability in large-scale electrocatalytic NRR.

We further compared the electrochemical performance of bimetallic Fe/Ni electrocatalysts with a range of different bimetallic compositions (Fig. 6a). FeNi₂-N-C, FeNi-N-C, Fe₂Ni-N-C and Fe₄Ni-N-C, show moderate NO₃⁻ conversion efficiency (54–71%) and N₂ selectivity (50–64%). These electrocatalytic results clearly indicate the optimized ratio of 3:1 (Fe:Ni) has the best relay catalytic effects to combine the adsorption and activation of both NO₃⁻ and the reaction intermediates during the NRR. Indeed, it is likely that the Fe catalytic sites perform the adsorption and activation of NO₃⁻, while the Ni centers contribute to the turnover of NO₂⁻ intermediate during NRR.²⁰ This conclusion was further confirmed by testing in the electrolyte containing 100 ppm NaNO₂-N and 0.1 M Na₂SO₄ at -1.3 V vs. SCE, and the results showed that Ni-N-C had a higher NO₂⁻ removal rate (65.2%) than Fe-N-C (13.1%). An increase in the metal ratio of Ni will result in more Ni[H], which can further reduce Ni[N₂] to Ni[NH], Ni[NH₂] and Ni[NH₃] through the sequential hydrogenerations. Therefore, the selectivity of N₂ may decrease with increasing metal ratio of Ni. Both removal of NO₃⁻ and N₂ selectivity simultaneously maximize at Fe/Ni = 3 due to that there are enough Fe sites for NO₃⁻ adsorption and reduction to NO₂⁻, and the amount of Ni [H] is enough to convert NO₂⁻ to N₂ while reducing Fe³⁺ to Fe.

The electrolysis tests were again performed under a variety of applied potential from -0.5 V to -1.7 V vs. SCE to investigate the best scenario for effective electrocatalytic NRR (Fig. 6b). No N₂ selectivity

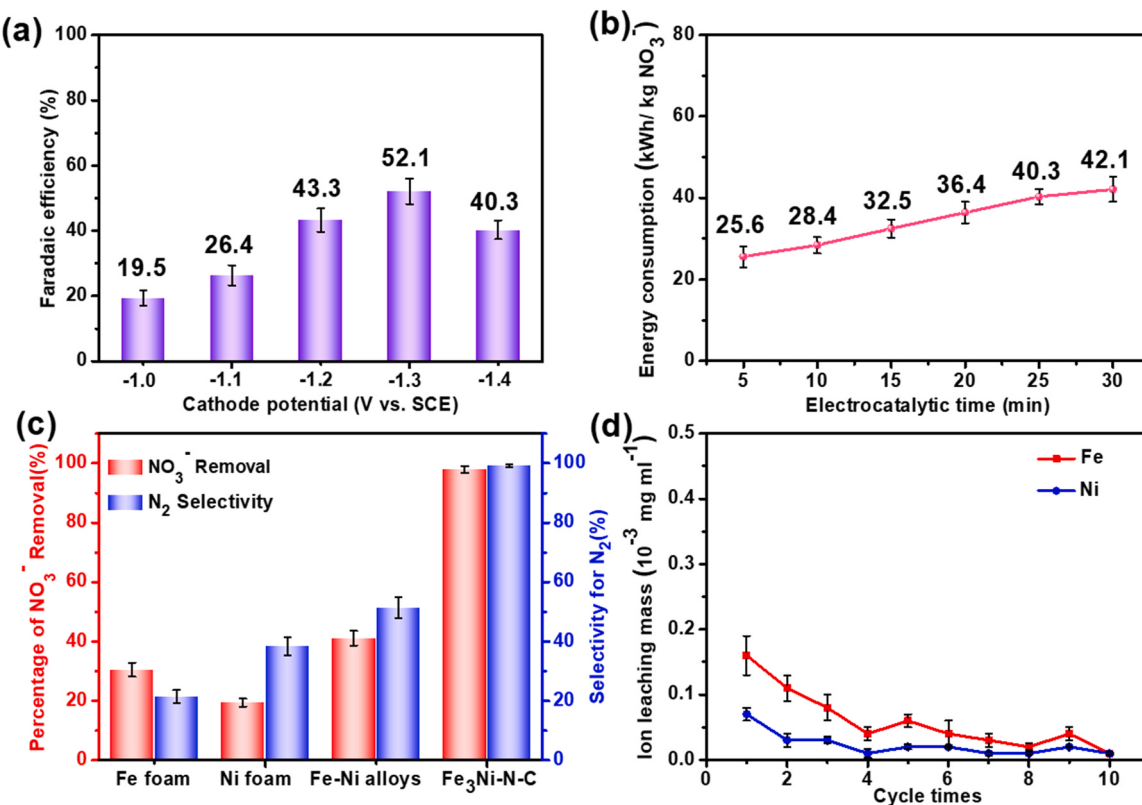


Fig. 5. (a) Faradaic efficiency under different applied cathode potentials. (b) Evolution of the specific Energy consumption during a 30 min electrolysis at a cathode potential of -1.3 V vs. SCE. (c) NO_3^- removal rate and N_2 selectivity of Fe foam, Ni foam, Fe-Ni alloys, and $\text{Fe}_3\text{Ni-N-C}$ electrodes. (d) The leaching mass of metal ions under 10 consecutive cycles of $\text{Fe}_3\text{Ni-N-C}$.

was obtained when the applied potential was -0.5 V vs. SCE, agreeing with the LSV results (Fig. 3a). The best NO_3^- removal rate (97.9%) and N_2 selectivity (99.3%) of $\text{Fe}_3\text{Ni-N-C}$ was achieved at -1.3 V vs. SCE, indicating that the NO_3^- reduction reaction could get enough energy at this potential and was less affected by the H_2 evolution reaction. Meanwhile, a decreased performance in both NO_3^- removal rate and N_2 selectivity was observed when the cathode potential exceeding -1.3 V vs. SCE, probably owing to the increasing competition from the H_2 evolution reaction [50]. We tested the production of hydrogen at a cathode potential of -1.3 V vs. SCE to be $80.7 \mu\text{mol}$ in 30 min (Fig. S17), and verified the mass and charge balance through charge calculations (Table S5).

Equally important to applied potentials is the initial pH of the electrolyte for electrocatalytic NRR. The electrolysis tests performed at different initial pH (3 ~ 11) show (Fig. 6c) high NO_3^- removal rate (94 ~ 98%) and N_2 selectivity (> 90%). These values confirm the electrocatalytic NRR on $\text{Fe}_3\text{Ni-N-C}$ are generic over a wide range of initial pH, and the highest NO_3^- to N_2 selectivity was achieved under neutral conditions (initial pH~7). The microporous framework structure is selective for the adsorption and transfer of surfactant species, and the short-range relay catalysis between bimetallics can weaken the influence of pH change. In addition, the DFT calculation results show that the unique FeNiN_6 coordination of the material greatly reduces the energy barrier for the reduction of NO_3^- to N_2 , which is why the material maintains excellent catalytic performance over a wide range of initial pH. The slightly increased NO_3^- removal rate under weakly acidic conditions (initial pH~5) was attributed to the promotion of conversion of NO_3^- to NH_4^+ . A decreased catalytic performance in NRR was reached in moderately acidic (initial pH~3) or alkaline (initial pH~11) conditions, which probably induce the competitive hydrogen evolution reaction and the adsorption of hydroxide, respectively [51]. To note, the best NRR performance of $\text{Fe}_3\text{Ni-N-C}$ is in the initial pH range of domestic

sewage (initial pH 7~8), suggesting the potential application of our electrocatalysts. Moreover, the excellent electrocatalytic performance of $\text{Fe}_3\text{Ni-N-C}$ was not decreased with variations in initial NO_3^- concentrations from $25 \text{ mg N/L} \sim 200 \text{ mg N/L}$ (Fig. 6d). The NO_3^- removal rate and N_2 selectivity were maintained to be over 91% and 90%, respectively [52,53].

The effects of these parameters on the electrocatalytic performance of NRR in a scale of 100 mL electrolyte were also investigated (Figs. S18–S20). $\text{Fe}_3\text{Ni-N-C}$ exhibited excellent NO_3^- removal capacity ($26,646 \text{ mgN g}^{-1}\text{FeNi h}^{-1}$), which was superior to all of the previous reported electrocatalysts (Table S4). However, the rate constant of nitrate reduction has an obvious decreasing trend with the decrease of the initial NO_3^- concentration (Fig. S19), which can be attributed to the weak binding strength with nitrate, reduced effective collision frequency of activated molecules and competitive adsorption with hydrogen under a lower NO_3^- concentration. Importantly, different concentrations of NaCl was added to the electrolyte to investigate the influence of the competing Cl^- concentration on NRR (Fig. S20). The electrocatalytic results showed no obvious effect on NO_3^- removal rate but even an increased N_2 selectivity from 89.9% to 99.5%. There are several reasons for the improvement of NO_3^- removal capacity: (1) Increased Cl^- concentration can improve the conductivity of electrolyte and promote ion transport. (2) The dissolved ammonia in the solution can further react with HClO to expose more effective active sites again. The dramatic increase in N_2 selectivity can be attributed to breakpoint chlorination. Chloride can be oxidized to form HClO , which oxidizes NH_4^+ to form N_2 (Eqs. (S8)–(S10)). This is further confirmed by the obvious change in colorimetric results of NH_4^+ upon NaCl (Fig. S20).

3.3. Proposed mechanism of nitrate reduction

In order to further investigate the origin of the excellent catalytic

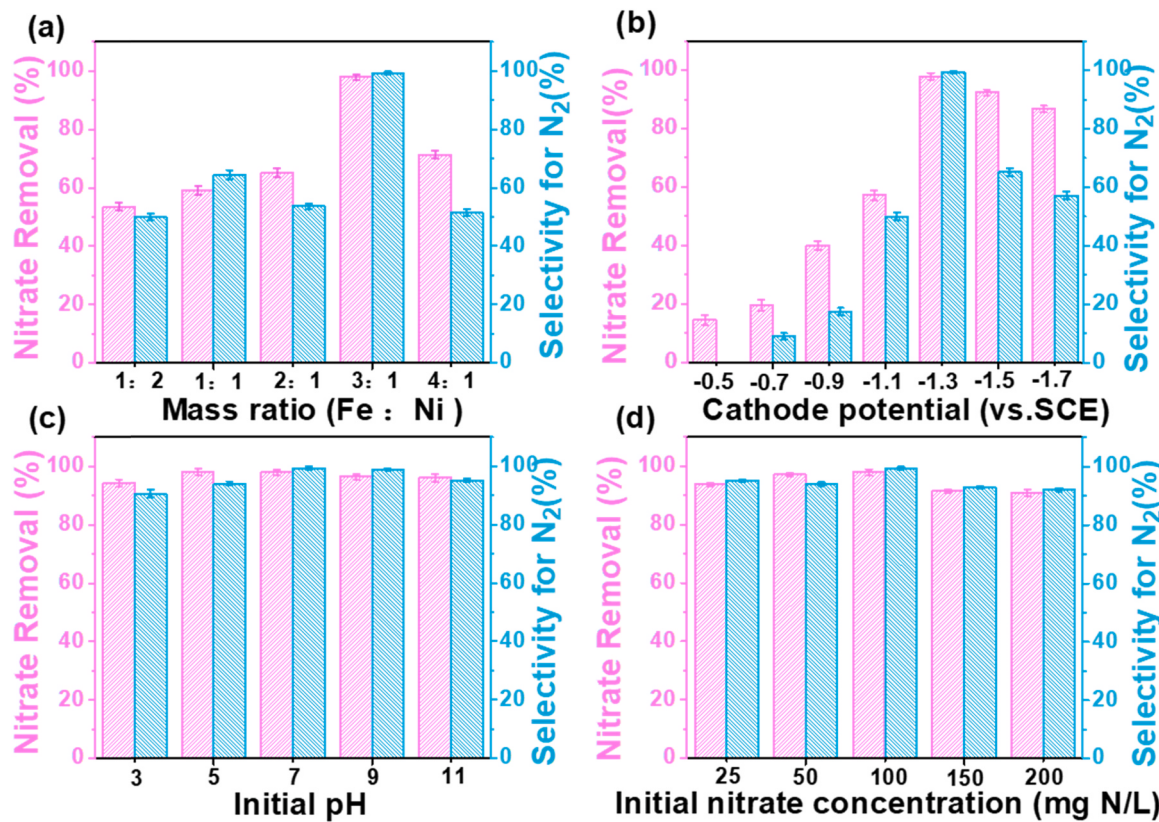
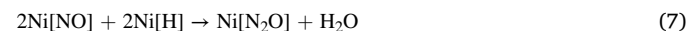
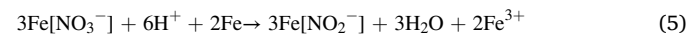


Fig. 6. Effects of (a) ratios of Fe to Ni, (b) applied potentials, (c) initial pH value and (d) initial NO₃⁻ concentrations on the NO₃⁻ removal rate and N₂ selectivity of Fe₃Ni-N-C (5 mL of electrolyte, 0.1 M Na₂SO₄, 30 min).

activity of Fe₃Ni-N-C and the mechanism of the NRR, a range of in-situ experiments and DFT calculations were carried out. Firstly, the electrochemical active surface areas (ECSA) of the catalysts were evaluated by electrochemical double-layer capacitance method (Figs. S21 and S22). The ECSA of Fe₃Ni-N-C (142.5 cm²) was larger than those of single metallic N-doped carbon materials (92.0 cm² of Fe-N-C and 75.3 cm² of Ni-N-C) as well as the parent N-doped carbon (32.8 cm²), therefore exhibiting more catalytic active sites. Importantly, the current density of Fe₃Ni-N-C was still higher than other cathodes after normalization of the polarization curve by ECSA (Fig. S23), indicating the intrinsic high catalytic activity of Fe₃Ni-N-C.

The intermediates and reaction pathways of Fe₃Ni-N-C in the electrocatalytic NRR were investigated by online differential electrochemical mass spectrometry (DEMS) and in-situ infrared (IR) tests. The signals with *m/z* values of 46 (NO₂), 30 (NO), 44 (N₂O), 28 (N₂) were detected through online DEMS in the applied potential range of 0 ~ -1.6 V vs. SCE during four continuous electrocatalytic cycles (Fig. 7a and b). The signal strength at *m/z* = 28 (N₂) is two orders of magnitude higher than that at *m/z* = 44 (N₂O). The large difference between the two signal strengths makes the signal at *m/z* = 28 which due to the fragmentation of N₂O approximately omitted, so we attribute the signal at *m/z* = 28 to N₂ [54]. Based on the DEMS results, the reaction pathways of nitrate electroreduction (NO₃⁻ → NO₂⁻ → NO → N₂O → N₂) were elucidated [55]. The signal of N₂ was detected at -1.0 V vs. SCE, which was lower than other three products, confirming the higher energy required for N₂ formation. The in-situ IR measurements of Fe₃Ni-N-C showed a substantial reduced intensity in the prominent stretching mode of NO₃⁻ (1064 and 1558 cm⁻¹) upon electrocatalysis at -1.3 V vs. SCE (Fig. 7c) [56]. Meanwhile, the concomitant enhanced intensity of new bands that are characteristic of NO₂⁻ (1125 cm⁻¹), NO* (1665 cm⁻¹) and N₂O* (2300 cm⁻¹) were observed [57-59]. These results suggest the reaction pathway of NO₃⁻ reduction to NO₂⁻, NO, and N₂O, respectively.

In addition, the influence of different applied potentials on the NRR was studied by in-situ IR studies (Fig. 7d). No apparent decrease in characteristic NO₃⁻ bands (1064 and 1558 cm⁻¹) was observed from applied potential of 0 V to -0.5 V vs. SCE, confirming the sluggish reduction process of NO₃⁻ to NO₂⁻ within this range of applied potentials. However, the applied potential from -0.5 V to -1.3 V will provide a substantial decrease in NO₃⁻ absorption bands (1064 and 1558 cm⁻¹) and the notable new peaks of NO₂⁻ (1125 cm⁻¹), NO* (1665 cm⁻¹), and N₂O* (2300 cm⁻¹), indicating the accelerated NO₃⁻ to N₂ process. The DEMS and in-situ IR tests imply the electrocatalytic NRR on Fe₃Ni-N-C involving following reaction pathways (Eqs. (4)-(9)):



NO₃⁻ is first reduced to NO₂⁻ by Fe with the oxidation of Fe to Fe³⁺, H₂ produced on the Fe₃Ni-N-C cathode can adsorb on the surface of Ni to form Ni[H]. The active Ni[H] can then reduce Fe³⁺ to Fe for continuing NO₃⁻ conversion to NO₂⁻. The extra Ni[H] can reduce NO₂⁻ to Ni[NO] and Ni[N₂O] step by step. N₂ can then be formed through the direct reduction of Ni[N₂O]. The tandem process and reaction energetics towards the electrocatalytic NRR were further studied by first-principles calculations. First, the inhibition effect of cathodes on hydrogen evolution reaction was investigated, which is a very important competitive side-reaction of NRR process (Fig. 7e). The energy barrier of H₂ generation on Fe₃Ni-N-C was 0.45 eV, which was essentially higher than that

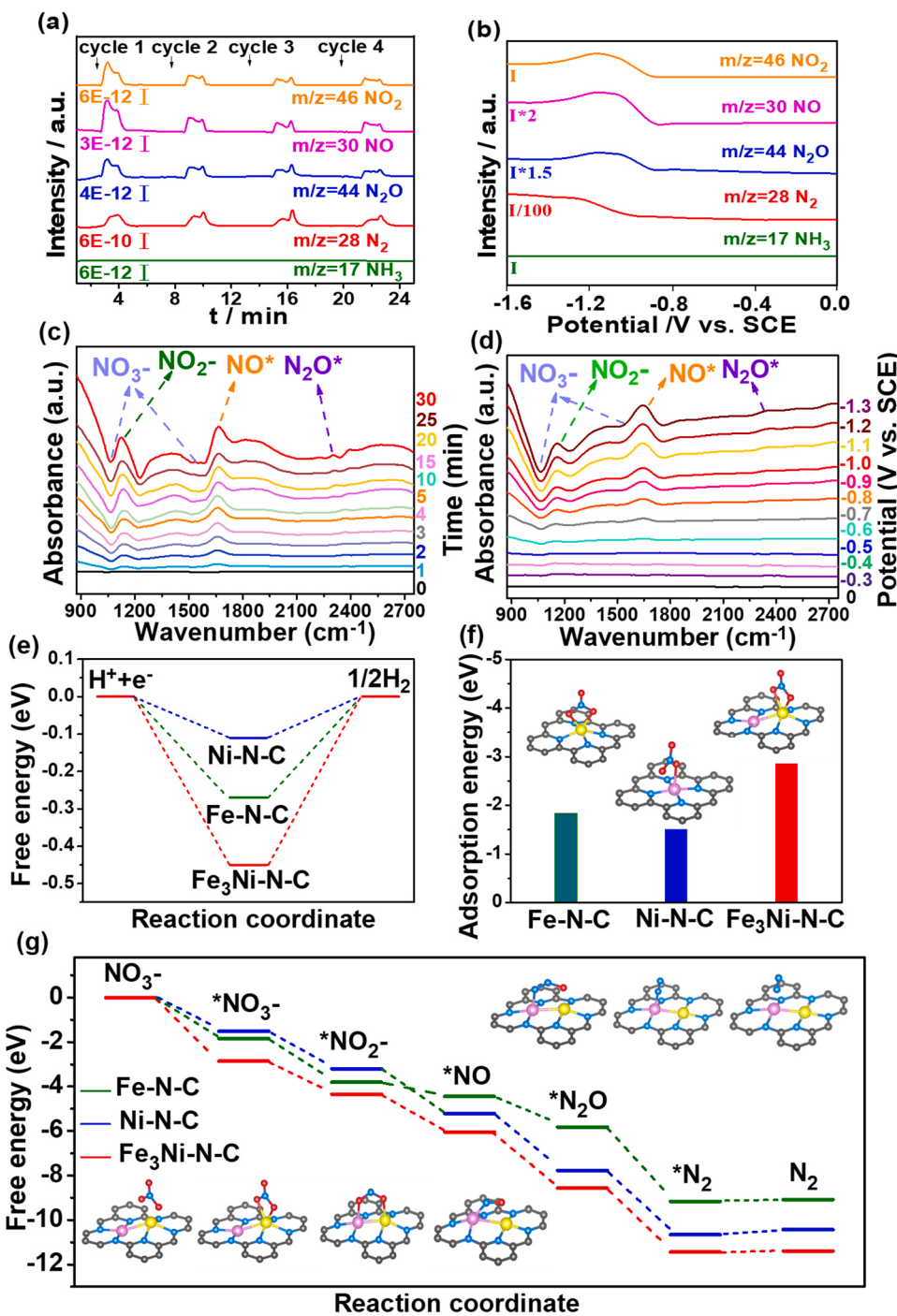


Fig. 7. (a,b) DEMS measurements of Fe₃Ni-N-C in electrocatalytic NRR. In-situ IR spectra of Fe₃Ni-N-C as a function of (c) reaction time and (d) the applied potential. (e) Reaction energies of H₂ formation, (f) reaction energies of NO₃⁻ adsorption and (g) free energy diagram of Fe₃Ni-N-C, Fe-N-C, and Ni-N-C. Molecular model (inset): C gray, N blue, Fe yellow, Ni purple, O red. (For interpretation of the references to color in this figure legend, the reader is referred to the web version of this article.)

of Fe-N-C (0.27 eV) and Ni-N-C (0.11 eV), confirming the bimetallic electrocatalysts less likely undergo the hydrogen evolution reaction [60]. In addition, the adsorption free energies of NO₃⁻ on the Fe sites of Fe₃Ni-N-C were calculated to be -2.85 eV, lower than the Fe sites of Fe-N-C (-1.84 eV) and the Ni site of Ni-N-C (-1.51 eV) (Fig. 7f). These calculated values confirm the synergistic effect of Fe-Ni bimetallic sites towards strong adsorption of NO₃⁻. Fig. 7g and Figs. S24-S26 showed the reaction path, structural models and free energies of each reaction state in the NRR, respectively. The free-energy diagram of the reaction pathway suggest the bimetallic Fe₃Ni-N-C exhibits the lowest energy state of every intermediate during the entire reaction process, evidencing its catalytic role in a more thermodynamic favorable process than the single metallic counterparts. To note, the structural model of

Ni-N-C after reduction of NO₃⁻ to NO* occupied a lower free energy than that of Fe-N-C, suggesting that the adsorption and activation of intermediates on the active Ni sites. In summary, DFT calculations show the thermodynamically more favorable NRR process on Fe₃Ni-N-C than other catalysts, and the important relay catalytic effects of Fe-Ni bimetallic species to the enhanced catalytic performance. Compared with the previous electrocatalytic nitrate reduction studies, this is the first report using advanced characterization techniques to achieve high N₂ selectivity and reveal detailed catalytic mechanism of electrochemical reduction NO₃⁻-to-N₂ (Table 1).

Table 1

Comparison of this work with other nitrate reduction reaction reported in literature.

Catalyst	Mass/Area of catalyst	Initial NO_3^- concentration	Volume (mL)	Time	Selectivity	Characterization	Reference
Co(III)-1,4,8,11-tetra-azacyclotetradecane	8 cm ²	0.1 M	25	/	NH_2OH (87%) NH_3 (3%) NO_2^- (12%)	CV ^b GC ^c	[61]
Pt	0.5–1 cm ²	0.1 M	/	2–20 min	NO_2^- (-) N_2 (-) NH_3 (-)	CV LSV	[24]
Pt-Ir alloy	0.5 mm in diameter	0.1 M	/	/	NO_2^- (-) NO (-) N_2O (-)	CV GC	[62]
Pt/Ru/Rh/Ir/Cu/Ag	/	0.1 M	/	/	NO_2^- (-) NO_2^- (-) N_2O (-) NH_3 (-) NH_2OH (-)	CV DEMS	[23]
Sn foil	6 cm ²	0.05 M	24	2.5 h	N_2 (92%) NH_3 (8%) NO_2^- (0.02%)	CV	[63]
$\text{Cu}_{80}\text{Ni}_{20}$ alloy	6 cm ²	0.02 M	/	4 h	NO_2^- (7.8%) NH_3 (85%) Other (7.2%)	CV	[64]
CuO nanowire arrays	1 cm ²	200 ppm NO_3^- -N	80	2 h	NH_3 (81.2%) Other (18.8%)	In-situ Raman DEMS DFT	[13]
Strained Ru nanoclusters	0.25 cm ²	1 M	/	100 h	NH_3 (~100%)	XAS ESR ^d DFT	[6]
Cu-3,4,9,10-perylenetetracarboxylic dianhydride	/	500 ppm NO_3^- -N	25	4 h	NO_2^- (-) NH_3 (-)	XAS DFT NMR ^e	[1]
Cu/Ni foam	12 cm ²	100 ppm NO_3^- -N	100	1 h	NO_2^- (-) NH_4^+ (-) N_2 (~100%)	LSV	[65]
Fe/Cu	12 cm ²	100 ppm NO_3^- -N	100	1.5 h	NO_2^- (-) NH_4^+ (-) N_2 (~100%)	UV-vis	[66]
$\text{Fe}_3\text{Ni-N-C}$	1 cm ²	100 ppm NO_3^- -N	5	30 min	N_2 (99.3%) Other (0.7%)	XAS DFT In-situ IR DEMS	Our work

a) “-” means no selectivity.

b) CV - Cyclic voltammogram.

c) GC - Gas chromatography.

d) ESR - Electron spin resonance.

e) NMR - Nuclear magnetic resonance.

4. Conclusion

We have successfully prepared a MOF-derived earth-abundant bimetallic porous carbon material to perform as an efficient, selective and long-term stable NRR electrocatalyst, achieving nearly quantitative conversion of NO_3^- to N_2 transformation within a short period of 30 min. Importantly, the electrocatalyst retains the high catalytic activity, when increasing the initial nitrate concentration, introducing Cl^- as the competing anion or tuning different initial pH (3 ~ 11). These control experiments show its potential in practical water purification applications. Online DEMS, in-situ IR and DFT calculations demonstrate multiple reaction pathways from NO_3^- to N_2 , which involves intermediates including NO_2^- , NO^* and N_2O^* . Our findings will open up a new avenue for MOF-derived NO_3^- reduction electrocatalysts based on the important design of earth-abundant multimetallic catalytic sites.

CRediT authorship contribution statement

Jie Sun: Conceptualization, Formal analysis, Methodology, Investigation, Data curation, Writing – original draft, Writing – review & editing. **Weiwei Gao:** Validation, Formal analysis, Investigation. **Hongyan Fei:** Writing – original draft, Validation. **Guohua Zhao:** Supervision, Conceptualization, Funding acquisition.

Declaration of Competing Interest

The authors declare that they have no known competing financial interests or personal relationships that could have appeared to influence the work reported in this paper.

Acknowledgements

We thank the staff of the 11B beamline at the Shanghai Synchrotron Radiation Facility (SSRF) for data collection. This work was supported by “National Natural Science Foundation of China” (NSFC, No. 21876128, 22076140, 21971197, 51772217, and U1932119), “National Key Basic Research Program of China” (2017YFA0403402) and the Shanghai Rising-Star Program (No. 20QA1409500). This work was also supported by Shanghai Large Scientific Facilities Center.

Appendix A. Supporting information

Supplementary data associated with this article can be found in the online version at doi:10.1016/j.apcatb.2021.120829.

References

- [1] G. Chen, Y. Yuan, H. Jiang, S. Ren, L. Ding, L. Ma, T. Wu, J. Lu, H. Wang, Electrochemical reduction of nitrate to ammonia via direct eight-electron transfer using a copper-molecular solid catalyst, *Nat. Energy* 5 (2020) 605–613.
- [2] Y. Wu, Z. Jiang, Z. Lin, Y. Liang, H. Wang, Direct electrosynthesis of methylamine from carbon dioxide and nitrate, *Nat. Sustain.* 4 (2021) 618–626, <https://doi.org/10.1038/s41893-021-00697-4>.
- [3] M. Duca, M.T.M. Koper, Powering denitrification: the perspectives of electrocatalytic nitrate reduction, *Energy Environ. Sci.* 5 (2012) 9726.
- [4] Y. Yao, S. Zhu, H. Wang, H. Li, M. Shao, A spectroscopic study of electrochemical nitrogen and nitrate reduction on rhodium surfaces, *Angew. Chem. Int. Ed.* 59 (2020) 10479–10483.
- [5] Y. Wang, A. Xu, Z. Wang, L. Huang, J. Li, F. Li, J. Wicks, M. Luo, D.H. Nam, C. S. Tan, Y. Ding, J. Wu, Y. Lum, C.T. Dinh, D. Sinton, G. Zheng, E.H. Sargent, Enhanced nitrate-to-ammonia activity on copper-nickel alloys via tuning of intermediate adsorption, *J. Am. Chem. Soc.* 142 (2020) 5702–5708.
- [6] J. Li, G. Zhan, J. Yang, F. Quan, C. Mao, Y. Liu, B. Wang, F. Lei, L. Li, A.W.M. Chan, L. Xu, Y. Shi, Y. Du, W. Hao, P.K. Wong, J. Wang, S. Dou, L. Zhang, J. Yu, Efficient

- ammonia electrosynthesis from nitrate on strained ruthenium nanoclusters, *J. Am. Chem. Soc.* 142 (2020) 7036–7046.
- [7] F. Yao, M. Jia, Q. Yang, F. Chen, Y. Zhong, S. Chen, L. He, Z. Pi, K. Hou, D. Wang, X. Li, Highly selective electrochemical nitrate reduction using copper phosphide self-supported copper foam electrode: performance, mechanism, and application, *Water Res.* 193 (2021), 116881.
- [8] S. Jia, P. Shi, Q. Hu, B. Li, T. Zhang, X. Zhang, Bacterial community shift drives antibiotic resistance promotion during drinking water chlorination, *Environ. Sci. Technol.* 49 (2015) 12271–12279.
- [9] W. Li, S. Patton, J.M. Gleason, S.P. Mezyk, K.P. Ishida, H. Liu, UV photolysis of chloramine and persulfate for 1, 4-dioxane removal in reverse-osmosis permeate for potable water reuse, *Environ. Sci. Technol.* 52 (2018) 6417–6425.
- [10] M.F. Haroon, S. Hu, Y. Shi, M. Imelfort, J. Keller, P. Hugenholtz, Z. Yuan, G. W. Tyson, Anaerobic oxidation of methane coupled to nitrate reduction in a novel archaeal lineage, *Nature* 500 (2013) 567–570.
- [11] J.C. Akunna, C. Bizeau, R. Moletta, Nitrate and nitrite reductions with anaerobic sludge using various carbon sources: glucose, glycerol, acetic acid, lactic acid and methanol, *Water Res.* 27 (1993) 1303–1312.
- [12] O. Einsle, A. Messerschmidt, R. Huber, P.M.H. Kroneck, F. Neese, Mechanism of the six-electron reduction of nitrite to ammonia by cytochrome c nitrite reductase, *J. Am. Chem. Soc.* 124 (2002) 11737–11745.
- [13] Y. Wang, W. Zhou, R. Jia, Y. Yu, B. Zhang, Unveiling the activity origin of a copper-based electrocatalyst for selective nitrate reduction to ammonia, *Angew. Chem. Int. Ed.* 59 (2020) 5350–5354.
- [14] W. Duan, G. Li, Z. Lei, T. Zhu, Y. Xue, C. Wei, C. Feng, Highly active and durable carbon electrocatalyst for nitrate reduction reaction, *Water Res.* 161 (2019) 126–135.
- [15] S.E. Braley, J. Xie, Y. Losovoj, J.M. Smith, Graphite conjugation of a macrocyclic cobalt complex enhances nitrite electroreduction to ammonia, *J. Am. Chem. Soc.* 143 (2021) 7203–7208.
- [16] Y. Wang, C. Wang, M. Li, Y. Yu, B. Zhang, Nitrate electroreduction: mechanism insight, in situ characterization, performance evaluation, and challenges, *Chem. Soc. Rev.* 50 (2021) 6720–6733, <https://doi.org/10.1039/d1cs00116g>.
- [17] P.H. van Langevelde, I. Katsounaros, M.T.M. Koper, Electrocatalytic nitrate reduction for sustainable ammonia production, *Joule* 5 (2021) 290–294.
- [18] S. Jung, S. Bae, W. Lee, Development of Pd–Cu/hematite catalyst for selective nitrate reduction, *Environ. Sci. Technol.* 48 (2014) 9651–9658.
- [19] J. Yao, Y. Mei, T. Yuan, J. Chen, H. Pan, J. Wang, Electrochemical removal of nitrate from wastewater with a Ti cathode and Pt anode for high efficiency and N2 selectivity, *J. Electroanal. Chem.* 882 (2021), 115019, <https://doi.org/10.1016/j.jelechem.2021.115019>.
- [20] X. Chen, T. Zhang, M. Kan, D. Song, J. Jia, Y. Zhao, X. Qian, Binderless and oxygen vacancies rich FeNi/graphitized mesoporous carbon/Ni foam for electrocatalytic reduction of nitrate, *Environ. Sci. Technol.* 54 (2020) 13344–13353.
- [21] C. Chen, K. Li, C. Li, T. Sun, J. Jia, Combination of Pd–Cu catalysis and electrolytic H2 evolution for selective nitrate reduction using protonated polypyrrole as a cathode, *Environ. Sci. Technol.* 53 (2019) 13868–13877.
- [22] C. Chen, H. Zhang, K. Li, Q. Tang, X. Bian, J. n Gu, Q. Cao, L. Zhong, C.K. Russell, M. Fan, J. Jia, Cu⁺ based active sites of different oxides supported Pd–Cu catalysts and electrolytic in-situ H2 evolution for high-efficiency nitrate reduction reaction, *J. Catal.* 392 (2020) 231–243.
- [23] G.E. Dima, A.C.A. de Vooy, M.T.M. Koper, Electrocatalytic reduction of nitrate at low concentration on coinage and transition-metal electrodes in acid solutions, *J. Electroanal. Chem.* 554 (2003) 15–23.
- [24] O.A. Petrii, T.Y. Safonova, Electroreduction of nitrate and nitrite anions on platinum metals: a model process for elucidating the nature of the passivation by hydrogen adsorption, *J. Electroanal. Chem.* 331 (1992) 897–912.
- [25] Y. Zhang, L. Jiao, W. Yang, C. Xie, H. Jiang, Rational fabrication of low-coordinate single-atom Ni electrocatalysts by MOFs for highly selective CO₂ reduction, *Angew. Chem. Int. Ed.* 60 (2021) 7607–7611.
- [26] S. Li, Y. Gao, N. Li, L. Ge, X. Bu, P. Feng, Transition metal-based bimetallic MOFs and MOF-derived catalysts for electrochemical oxygen evolution reaction, *Energy Environ. Sci.* 14 (2021) 1897–1927.
- [27] H. Furukawa, K.E. Cordova, M. O’Keeffe, O.M. Yaghi, The chemistry and applications of metal–organic frameworks, *Science* 341 (2013) 974, <https://doi.org/10.1126/science.1230444>.
- [28] W. Ren, X. Tan, W. Yang, C. Jia, S. Xu, K. Wang, S.C. Smith, C. Zhao, Isolated diatomic Ni–Fe metal–nitrogen sites for synergistic electroreduction of CO₂, *Angew. Chem. Int. Ed.* 58 (2019) 6972–6976.
- [29] J. Lee, O.K. Farha, J. Roberts, K.A. Scheidt, S.T. Nguyen, J.T. Hupp, Metal–organic framework materials as catalysts, *Chem. Soc. Rev.* 38 (2009) 1450–1459.
- [30] Z. Liang, C. Qu, D. Xia, R. Zou, Q. Xu, Atomically dispersed metal sites in MOF-based materials for electrocatalytic and photocatalytic energy conversion, *Angew. Chem. Int. Ed.* 57 (2018) 9604–9633.
- [31] S. Zhao, Y. Wang, J. Dong, C. He, H. Yin, P. An, K. Zhao, X. Zhang, C. Gao, L. Zhang, J. Lv, J. Wang, J. Zhang, A.M. Khattak, N.A. Khan, Z. Wei, J. Zhang, S. Liu, H. Zhao, Z. Tang, Ultrathin metal–organic framework nanosheets for electrocatalytic oxygen evolution, *Nat. Energy* 1 (2016) 16184.
- [32] L. Majidi, A. Ahmadiparidari, N. Shan, S.N. Misal, K. Kumar, Z. Huang, S. Rastegar, Z. Hemmat, X. Zou, P. Zapol, J. Cabana, L.A. Curtiss, A. Salehi-Khojin, 2D copper tetrahydroxyquinone conductive metal–organic framework for selective CO₂ electrocatalysis at low overpotentials, *Adv. Mater.* 33 (2021), e2004393.
- [33] H. Zhang, W. Xia, H. Shen, W. Guo, Z. Liang, K. Zhang, Y. Wu, B. Zhu, R. Zou, Antiperovskite intermetallic nanoparticles for enhanced oxygen reduction, *Angew. Chem. Int. Ed.* 59 (2020) 1871–1877.
- [34] G. Meng, H. Tian, L. Peng, Z. Ma, Y. Chen, C. Chen, Z. Chang, X. Cui, J. Shi, Ru to W electron donation for boosted HER from acidic to alkaline on Ru/WNO sponges, *Nano Energy* 80 (2021), 105531.
- [35] J. Hafner, Ab-initio simulations of materials using VASP: density-functional theory and beyond, *Comput. Chem.* 29 (2008) 2044–2078.
- [36] Y. Lin, G. Li, S. Mao, J. Chai, Long-range corrected hybrid density functionals with improved dispersion corrections, *J. Chem. Theory Comput.* 9 (2013) 263–272.
- [37] A.D. Handoko, F. Wei, Jenndy, B.S. Yeo, Z.W. Seh, Understanding heterogeneous electrocatalytic carbon dioxide reduction through operando techniques, *Nat. Catal.* 1 (2018) 922–934.
- [38] D.H. Ha, B. Han, M. Risch, L. Giordano, K.P.C. Yao, P. Karayalali, Y. Shao-Horn, Activity and stability of cobalt phosphides for hydrogen evolution upon water splitting, *Nano Energy* 29 (2016) 37–45.
- [39] N. Heck, B.G. Janesko, G.E. Scuseria, N.J. Halas, M.S. Wong, Using catalytic and surface-enhanced Raman spectroscopy-active gold nanoshells to understand the role of basicity in glycerol oxidation, *ACS Catal.* 3 (2013) 2430–2435.
- [40] X. Huang, Y. Lin, J. Zhang, X. Chen, Ligand-directed strategy for zeolite-type metal–organic frameworks: zinc (II) imidazolates with unusual zeolitic topologies, *Angew. Chem. Int. Ed.* 45 (2006) 1557–1559.
- [41] F. Pan, H. Zhang, K. Liu, D. Cullen, K. More, M. Wang, Z. Feng, G. Wang, G. Wu, Y. Li, Unveiling active sites of CO₂ reduction on nitrogen-coordinated and atomically dispersed iron and cobalt catalysts, *ACS Catal.* 8 (2018) 3116–3122.
- [42] C. Zhao, X. Dai, T. Yao, W. Chen, X. Wang, J. Wang, J. Yang, S. Wei, Y. Wu, Y. Li, Ionic exchange of metal–organic frameworks to access single nickel sites for efficient electroreduction of CO₂, *J. Am. Chem. Soc.* 139 (2017) 8078–8081.
- [43] H. Yang, S. Hung, S. Liu, K. Yuan, S. Miao, L. Zhang, X. Huang, H. Wang, W. Cai, R. Chen, J. Gao, X. Yang, W. Chen, Y. Huang, H. Chen, C. Li, T. Zhang, B. Liu, Atomically dispersed Ni (I) as the active site for electrochemical CO₂ reduction, *Nat. Energy* 3 (2018) 140–147.
- [44] J. Wang, Z. Huang, W. Liu, C. Chang, H. Tang, Z. Li, W. Chen, C. Jia, T. Yao, S. Wei, Y. Wu, Y. Li, Design of N-coordinated dual-metal sites: a stable and active Pt-free catalyst for acidic oxygen reduction reaction, *J. Am. Chem. Soc.* 139 (2017) 17281–17284.
- [45] S. Kabir, K. Artyushkova, B. Kiefer, P. Atanassov, Computational and experimental evidence for a new TM–N3/C moiety family in non-PGM electrocatalysts, *Phys. Chem. Chem. Phys.* 17 (2015) 17785–17789.
- [46] V. Rosca, M. Duca, M.T. de Groot, M.T.M. Koper, Nitrogen cycle electrocatalysis, *Chem. Rev.* 109 (2009) 2209–2244.
- [47] K. Yang, J. Liu, B. Yang, Mechanism and active species in NH₃ dehydrogenation under an electrochemical environment: an Ab initio molecular dynamics study, *ACS Catal.* 11 (2021) 4310–4318.
- [48] M. Chen, H. Wang, Y. Zhao, W. Luo, L. Li, Z. Bian, L. Wang, W. Jiang, J. Yang, Achieving high-performance nitrate electrocatalysis with PdCu nanoparticles confined in nitrogen-doped carbon coralline, *Nanoscale* 10 (2018) 19023–19030.
- [49] Y.J. Shih, Z. Wu, C. Lin, Y. Huang, C. Huang, Manipulating the crystalline morphology and facet orientation of copper and copper–palladium nanocatalysts supported on stainless steel mesh with the aid of cationic surfactant to improve the electrochemical reduction of nitrate and N2 selectivity, *Appl. Catal. B Environ.* 273 (2020), 119053.
- [50] R. Mao, H. Lan, L. Yan, X. Zhao, H. Liu, J. Qu, Enhanced indirect atomic H^{*} reduction at a hybrid Pd/graphene cathode for electrochemical dechlorination under low negative potentials, *Environ. Sci. Nano* 5 (2018) 2282–2292.
- [51] J. Liu, T. Cheng, L. Jiang, A. Kong, Y. Shan, Efficient nitrate reduction over novel covalent Ag-salophen polymer-derived “Vein-Leaf-Apple”-like Ag@carbon structures, *ACS Appl. Mater. Interfaces* 12 (2020) 33186–33195.
- [52] L. Su, D. Han, G. Zhu, H. Xu, W. Luo, L. Wang, W. Jiang, A. Dong, J. Yang, Tailoring the assembly of iron nanoparticles in carbon microspheres toward high-performance electrocatalytic denitrification, *Nano Lett.* 19 (2019) 5423–5430.
- [53] W. Teng, N. Bai, Y. Liu, Y. Liu, J. Fan, W. Zhang, Selective nitrate reduction to dinitrogen by electrocatalysis on nanoscale iron encapsulated in mesoporous carbon, *Environ. Sci. Technol.* 52 (2018) 230–236.
- [54] Y. Lan, J. Chen, H. Zhang, W. Zhang, J. Yang, Fe/Fe₃C nanoparticle-decorated N-doped carbon nanofibers for improving the nitrogen selectivity of electrocatalytic nitrate reduction, *J. Mater. Chem. A* 8 (2020) 15853–15863.
- [55] S. Garcia-Segura, M. Lanzarini-Lopes, K. Hristovski, P. Westerhoff, Electrocatalytic reduction of nitrate: fundamentals to full-scale water treatment applications, *Appl. Catal. B Environ.* 236 (2018) 546–568.
- [56] S. Shang, C. Yang, Y. Tian, Z. Tao, A. Hanif, M. Sun, H.H.S. Wong, C. Wang, J. Shang, NO₂ removal by adsorption on transition-metal-based layered double hydroxides, *ACS EST Eng.* 1 (2020) 375–384.
- [57] L. Sivachandiran, F. Thevenet, A. Rousseau, D. Bianchi, NO₂ adsorption mechanism on TiO₂: an in-situ transmission infrared spectroscopy study, *Appl. Catal. B Environ.* 198 (2016) 411–419.
- [58] H. Wang, Y. Sun, G. Jiang, Y. Zhang, H. Huang, Z. Wu, S.C. Lee, F. Dong, Unraveling the mechanisms of visible light photocatalytic NO purification on earth-abundant insulator-based core–shell heterojunctions, *Environ. Sci. Technol.* 52 (2018) 1479–1487.
- [59] A. Filtschew, P. Beato, S.B. Rasmussen, C. Hess, The role of platinum on the NO_x storage and desorption behavior of ceria: an online FT-IR study combined with in situ Raman and UV-vis spectroscopy, *Phys. Chem. Chem. Phys.* 23 (2021) 1874–1887.
- [60] P. Li, M. Wang, X. Duan, L. Zheng, X. Cheng, Y. Zhang, Y. Kuang, Y. Li, Q. Ma, Z. Feng, W. Liu, X. Sun, Boosting oxygen evolution of single-atomic ruthenium through electronic coupling with cobalt–iron layered double hydroxides, *Nat. Commun.* 10 (2019) 1711.

- [61] N. Taniguchi, K. Nakashima, K. Yasukouchi Matsushita, Electrocatalytic reduction of nitrate and nitrite to hydroxylamine and ammonia using metal cyclams, *J. Electroanal. Chem.* 224 (1987) 199–209.
- [62] S. UretaZanartu, C. Yanez, Electroreduction of nitrate ion on Pt, Ir and on 70:30 Pt:Ir alloy, *Electrochim. Acta* 42 (1997) 1725–1731.
- [63] D. Katsounaros, C. Ipsakis, G.Kyriacou Polatides, Efficient electrochemical reduction of nitrate to nitrogen on tin cathode at very high cathodic potentials, *Electrochim. Acta* 52 (2006) 1329–1338.
- [64] L. Mattarozzi, S. Cattarin, N. Comisso, P. Guerriero, M. Musiani, L. Vazquez-Gomez, E. Verlato, Electrochemical reduction of nitrate and nitrite in alkaline media at CuNi alloy electrodes, *Electrochim. Acta* 89 (2013) 488–496.
- [65] Y. Zhang, Y. Zhao, Z. Chen, L. Wang, P. Wu, F. Wang, Electrochemical reduction of nitrate via Cu/Ni composite cathode paired with Ir-Ru/Ti anode: high efficiency and N₂ selectivity, *Electrochim. Acta* 291 (2018) 151–160.
- [66] Y. Zhang, Y. Zhao, Z. Chen, L. Wang, L. Zhou, P. Wu, F. Wang, P. Qu, Fe/Cu composite electrode prepared by electrodeposition and its excellent behavior in nitrate electrochemical removal, *J. Electrochem. Soc.* 165 (2018) E420–E428.